Structure and Properties of the $Sr_2In_{1-x}Sn_xSbO_6$ Double Perovskite

Lun Jin[1, *], Danrui Ni[1], Xin Gui[1], Tai Kong[2], Duncan H. Moseley[3], Raphael P. Hermann[3] and Robert J. Cava[1, *]

[1]Department of Chemistry, Princeton University, Princeton, NJ, 08544, USA
[2]Department of Physics, University of Arizona, Tucson, AZ, 85721, USA

[3]Materials Science and Technology Division, Oak Ridge National Laboratory, Oak Ridge, Tennessee 37831, USA

***** E-mails of corresponding authors: ljin@princeton.edu; rcava@princeton.edu

***Keywords*:** cation-ordered double perovskites, *n*-type semiconductors, X-ray powder diffraction, Mössbauer spectroscopy, band gaps, band structures

Abstract: A series of *n*-type oxide double perovskite semiconductors, $Sr_2In_{1-x}Sn_xSbO_6$ $(0 \leq x \leq 0.3)$ has been synthesized; Sn^{4+} partially substitutes for In^{3+}. ^{121}Sb and ^{119}Sn Mössbauer spectroscopy are employed to investigate the B-site cation ordering because this issue cannot be resolved by conventional diffraction techniques alone. Rigid ordering between In^{3+}/Sn^{4+} and Sb^{5+} sites is revealed by the spectroscopic method, and hence in combination with the structural parameters extracted from the XRD structural refinements, the crystallographic structure of this series of compounds is depicted. The temperature dependent magnetic susceptibilities, band gaps, and carrier type are characterized, and the calculated band structure is presented.

1. Introduction

Complex metal oxides continue to be the subject of study in materials chemistry and condensed-matter physics in part because they possess a wide variety of physical and chemical properties.[1–5] Perovskites are one of the most important families in complex metal oxides, since they can accommodate a wide range of elements and are particularly integrable into next-generation devices.[6–9] Hence, oxide perovskite semiconductors can potentially provide an alternative to the traditional semiconductors based on main group elements that have been widely employed in current information technology.

Owing to their remarkable structural stability and tolerance for many ions, oxide perovskite semiconductors often survive chemical doping. Based on the type of dopant introduced into the system, extrinsic oxide perovskite semiconductors can be either *n*-type or *p*-type. *N*-type semiconductors are created by electron donor dopants, such as introducing Group IV element into a bulk phase of Group III element, hence adding electrons into the conduction band. In contrast, *p*-type semiconductors are created by electron acceptor dopants, thus holes in the valence band can be created by adding Group IV element into a bulk phase of Group V element.

Sr_2InSbO_6 adopts a double perovskite structure with alternating BO_6-$B'O_6$ octahedra, where the charge difference of 2 units and contrast in ionic radii of In^{3+} (0.94 Å) and Sb^{5+} (0.74 Å) make cation ordering preferred on the perovskite B-site. Several early studies claimed the material to simply display a doubled cubic unit cell, ($a \approx 2a_p$, with a_p denoting the lattice parameter of a single cubic perovskite cell.[10–12]) but two recent reports found the symmetry of this phase to be slightly distorted from cubic, crystallizing in the monoclinic space group $P2_1/n$ ($a \approx b \approx \sqrt{2}a_p$, $c \approx 2a_p$, $\beta \approx 90°$).[13,14] The latter two reports, although agreeing in general,

disagree in a subtle way - regarding whether there is complete or partial cation ordering between In^{3+} and Sb^{5+} on the B sites.

In this study, Sn^{4+} was employed to partially substitute for In^{3+} in Sr_2InSbO_6. Ignoring for the moment the possibility of small amounts of intrinsic In-Sb disorder, the addition of the 3rd B-site element may lead to total B-site disorder in the system. Considering the close X-ray form factors, which are essentially determined by the atomic numbers, and the similarity of neutron scattering lengths (In (4.065 fm), Sn (6.225 fm), and Sb (5.57 fm)) of the B-site cations, techniques other than diffraction are also needed to best determine the crystal structures of the $Sr_2In_{1-x}Sn_xSbO_6$ ($0 \leq x \leq 0.3$) double perovskite series. In the following we describe our ^{121}Sb and ^{119}Sn Mössbauer spectroscopy studies to shed light on this issue. Physical properties of these materials including magnetism, band gaps and band structures, and type of carriers are fully characterized in this study as well.

2. Experimental

Approximately 2.0 g polycrystalline powder samples of $Sr_2In_{1-x}Sn_xSbO_6$ ($0 \leq x \leq 0.5$) double perovskites were prepared via conventional high-temperature ceramic synthesis. Stoichiometric metal ratios of $SrCO_3$ (Alfa Aesar, 99.99%), In_2O_3 (Alfa Aesar, 99.99%), Sb_2O_5 (Alfa Aesar, 99.998%) and SnO_2 (Alfa Aesar, 99.9%) were ground together using an agate mortar and pestle, and then transferred into an alumina crucible. These reaction mixtures were first slowly (1 °C/min) heated to 1000 °C in air and held overnight to decompose the carbonate, and then were directly annealed in air at 1500 °C (3 °C/min) for 2 periods of 48 hours with intermittent grindings. The reaction progress was monitored using laboratory X-ray powder diffraction data collected at room temperature on a Bruker D8 FOCUS diffractometer (Cu Kα) over a 2θ range between 5° and 70°.

Once the reactions were complete, laboratory XRD data with much better statistical significance, covering a 2θ range between 5° and 110°, were collected from each sample. Lattice parameters, atomic positions, and atomic displacement factors using these data were determined by the Rietveld method[15] using the GSAS-II program.

Room temperature Mössbauer spectra of polycrystalline samples of $Sr_2In_{1-x}Sn_xSbO_6$ (x = 0, 0.1, 0.2, 0.3) were measured using the ^{121}Sb and ^{119}Sn Mössbauer transitions. For each sample, 125 mg of powdered material was mixed with boron nitride and sandwiched between Kapton tape in a 12.5 mm diameter sample holder, for a 102 mg/cm^2 thickness. ^{121}Sb and ^{119}Sn Mössbauer spectra were recorded with a 0.5 mCi Ca $^{121m}SnO_3$ and a 0.1 mCi $Ca^{119m}SnO_3$ source, respectively. The velocity transducer was operated in constant acceleration mode and calibrated using an *a*-iron Mössbauer spectrum with a ^{57}Co@Rh source. Isomer shifts and spectra are reported relative to $CaSnO_3$.

The magnetization data were collected using the ACMS II and VSM option of a Quantum Design Physical Property Measurement System (PPMS). Temperature-dependent magnetization (M) data were collected from finely ground powders in an applied field (H) of 9 T. The magnetic susceptibility χ was defined as M (in emu)/H (in Oe). Field-dependent magnetization data between H = 0 Oe and 90000 Oe were collected at T = 300 K and 1.8 K.

The diffuse reflectance spectra were collected from powder samples at ambient temperature on a Cary 5000i UV-VIS-NIR spectrometer equipped with an internal DRA-2500 integrating sphere. The data were converted from reflectance to pseudo-absorbance using the Kubelka-Munk method, and values of band transitions were calculated from Tauc plots.[16]

The band structures and electronic densities of states (DOS) were calculated using the WIEN2k program. The full-potential linearized augmented plane wave (FP-LAPW) method with local orbitals was used.[17,18] Electron correlation was treated via the generalized gradient

approximation.[19] The conjugate gradient algorithm was applied, and the energy cutoff was set at 500 eV. Reciprocal space integrations were completed over a 6×6×4 Monkhorst-Pack *k*-point mesh.[20] Spin-orbit coupling (SOC) effects were applied for the In and Sb atoms. The crystallographic data were obtained from W.T. Fu *et al*.[13] The calculated total energy converged to less than 0.1 meV per atom.

3. Results and Discussion

3.1 Structural Characterization

Laboratory X-ray powder diffraction (pXRD) data were collected from each composition. The stacked profile of lab pXRD data (Figure 1a) simply indicates that the sample's homogeneity is maintained until 30% Sn^{4+}-for-In^{3+} substitution. Beyond this composition threshold, an orthorhombic secondary phase, $Sr_2Sb_2O_7$, starts to occur, as illustrated by the growth of the non-perovskite peaks highlighted in Figure 1a. To further characterize the result of the doping, the lattice parameters of single-phase samples of $Sr_2In_{1-x}Sn_xSbO_6$ ($0 \leq x \leq 0.3$) were extracted from Rietveld refinements of the lab pXRD data and plotted against the doping level *x* (Figure 1b). This confirms that the substitution was successful. Given that the ionic radii of In^{3+} and Sn^{4+} are 0.94 Å and 0.83 Å respectively, the observed shrunken lattice parameters *a*, *b*, *c* and cell volume *V* with respect to increasing Sn doping level are as expected for Sn^{4+} substitution on the In^{3+} site. (The very small errors on the refined lattice parameters are known to be more significant statistically than to have real physical meaning.) In addition, although the change is quite subtle, the angle β does progress towards 90° with more Sn^{4+} substituted into the lattice, indicating that the monoclinic unit cell is less distorted (discussed in detail at the end of this section).

Structural characterizations were performed by refining laboratory pXRD data against the structure of the parent phase Sr_2InSbO_6, with the all-In^{3+} site replaced by $In^{3+}_{1-x}Sn^{4+}_{x}$. All refinements converged smoothly and provided satisfactory agreement parameters. Observed, calculated and difference plots from the Rietveld refinement of $Sr_2In_{0.9}Sn_{0.1}SbO_6$ (space group $P2_1/n$) against the lab pXRD data are shown in Figure 2a, and the crystal structure together with selected bond lengths for the SbO_6 octahedron and the $(In/Sn)O_6$ octahedron, are depicted in Figure 2b as a representative, while the rest can be found in Figures S1-S3. The structural parameters and crystallographic positions of $Sr_2In_{0.9}Sn_{0.1}SbO_6$ thus determined are presented in Table 1 and those of the remaining compositions can be found in Tables S1-S3. (The extremely similar X-ray form factors for the B-site cations indicate that the atomic fractions must be fixed to their nominal values during the structure refinements. The high purity starting reagents, the existence of a single monoclinic phase and the single-site occupancy determined by the Mössbauer data (discussed in the following) all ensure the nominal fractions of Sn and In in our samples.) The results show that the SbO_6 octahedron is significantly smaller in size than the $(In/Sn)O_6$ octahedron, as evidenced by selected bond lengths for these two octahedra (Figure 2b). If the rigid B-site cation ordering between In^{3+}/Sn^{4+} and Sb^{5+} is not conserved, i.e., that these cations are scrambled by the Sn occupancy, then ^{121}Sb and ^{119}Sn Mössbauer spectroscopy should be able to tell whether this is the case due to the consequence of distinguished coordination environments.

Given that conventional diffraction techniques are not sufficiently sensitive to fully depict the B-site cation ordering in our materials, ^{121}Sb and ^{119}Sn Mössbauer spectra serve well for that purpose – providing data that supplements the unit cell parameters extracted from the pXRD structural refinements. This spectroscopic technique confirms the occupancy of the corresponding cations, revealing substitution of the Sn for the In, with the Sb site preserved, thus ultimately specifying

the crystallographic structure of our materials and aiding in the understanding of the physical properties, which are discussed in the following section.

A recent study reported the success of using the ^{119}Sn Mössbauer spectrum to characterize two crystallographically independent Sn sites in the crystal structure of the diamagnetic birefringent material $Sn_2B_5O_9Cl$[21]; showing that ^{121}Sb and ^{119}Sn Mössbauer spectroscopy should be sensitive enough to distinguish single Sb/Sn site occupancy from double Sb/Sn site occupancy in our materials as well. Reasonable signal strength is expected at room temperature considering the U_{iso} from XRD, which lead to a recoil-free fraction, $f_{LM} = \exp(-k^2.U_{iso})$ of 0.37 and 0.80 for ^{121}Sb and ^{119}Sn, respectively; k is E/ħc, the momentum of the Mössbauer γ-ray. Hence room temperature Mössbauer spectra of polycrystalline samples of $Sr_2In_{1-x}Sn_xSbO_6$ ($0 \leq x \leq 0.3$) were measured using the ^{121}Sb and ^{119}Sn Mössbauer transitions. The Mössbauer spectra in Figure 3a exhibit a single line absorption both for ^{121}Sb and ^{119}Sn. The solid lines correspond to a single-site fit of each dataset, with the ^{121}Sb data for the undoped $x = 0$ parent phase centered around 0.11(1) mm/s and all ^{119}Sn data centered around 0.000(4) mm/s. These isomer shifts are as expected for tetravalent tin and for pentavalent antimony[22–24]. All spectral quantities are reported with their error bars in Figure 3b.

For Sb-Mössbauer, the linewidth remains relatively constant with doping, around $\Gamma = 3$ mm/s. This value is intrinsically fairly large, and for a small distribution of the local environment the linewidth will not be highly sensitive, in particular as far as only the non-Sb site metal centers are impacted by the substitution of In by Sn. The quadrupole splitting and isomer shifts both clearly decrease with doping from ΔE_Q = -1.4(4) to -2.4(3) mm/s and δ = 0.11(1) to 0.03(1) mm/s, respectively (Figure 3b). Note that the quadrupole splitting witnesses the local distortion. For Sb, it increases in magnitude, indicating an increase in site distortion for Sb upon doping as its nearest-neighbor

metal centers used to constitute pure In is now disturbed by substituting Sn for In. The decrease in isomer shift indicates a small increase in the local electron density around the ^{121}Sb nucleus. The 0.3 electrons per formula unit added upon replacing 30% of the In present with Sn adds 0.006(1) *s* electrons to Sb, when using the trends outlined in previous work[23]. While fitting, we have compared models with an asymmetry parameter of the electric field gradient, $\eta = (V_{xx}-V_{yy})/V_{zz}$, by fitting with η = 0 and 1, where η = 1 produced lower errors and clearer trends in the fitted parameters, indicating a slight distortion in the electron density in the plane perpendicular to V_{zz}.

In the Sn-Mössbauer spectra (Figure 3b), the isomer shift is relatively constant at 0.000(4) mm/s. In contrast, the linewidth increases with doping from 0.83(3) to 0.88(1) mm/s. It is indeed much narrower compared to that in Sb-Mössbauer (3 mm/s) and thus more sensitive towards a small distribution of local environment. The quadrupole splitting increases from 0.37(2) to 0.48(1) mm/s, also indicating an increase in site distortion upon doping[24]. The increase in both the linewidth and the quadrupole splitting with increasing Sn content can be rationalized as being due to a gradual change in the binomial distribution probability of a specific Sn having no next-nearest-neighbor Sn centers for low Sn content, to increasingly higher probabilities of having zero, one, or more of their next-near-neighbor In centers being substituted. In addition, the variations in the quadrupole splitting in Sn-Mössbauer are smaller compared to those in Sb-Mössbauer as they are brought by the modifications of next-nearest-neighbor metal centers, thus we cannot further assess these effects more quantitatively.

A side-view of the unit cell along the *b* axis is depicted in Figure 4. In this case, the β angle (in the *ac*-plane) is directly affected by the local distortion of the conjugated MO_6 octahedra within the monoclinic unit cell. Both SbO_6 and $(In/Sn)O_6$ octahedra become more distorted upon increasing Sn concentration, as illustrated by the increase in magnitude of quadrupole splitting in ^{121}Sb and

^{119}Sn Mössbauer spectra. Hence it causes the Sb–O3–(In/Sn) chain along the *c* axis to become more bent (the bond angle decreases) while the Sb and (In/Sn) atoms remain sitting on their special positions. Consequently, the O1 and O2 atoms that link the Sb and (In/Sn) atoms along the *a* axis have to be "pushed out". This effectively causes the *a* axis to move farther from the *c* axis, making the β angle, although very subtle, less deviated from 90°. Therefore the monoclinic unit cell is less distorted.

3.2 Property Characterization

3.2.1 Magnetic Properties

The temperature-dependent magnetization data were collected for each composition of the $Sr_2In_{1-x}Sn_xSbO_6$ ($0 \leq x \leq 0.3$) series under an applied field of H = 9 T and then plotted as magnetic susceptibility χ (M/H) against temperature T (Figure 5a). All of the phases are diamagnetic in the bulk material as evidenced by the magnetic susceptibility curves being below zero. The magnetic susceptibility consists of a relatively temperature-independent part ($100 \leq T$ / K ≤ 300) and an upward-pointing tail as is commonly seen in the low-temperature regime. The field-dependent magnetization data are collected from each phase at T = 300 K and 1.8 K and plotted as M against H ($0 \leq H$ / T ≤ 9) in Figure 5b & c, respectively. The magnetization data collected at 300 K as a function of applied field is linear in the whole range with a negative slope, while analogous data collected at 1.8 K shows a curvature in the low-field regime and progresses linearly with a negative slope against the applied field afterwards, all consistent with the temperature-dependent magnetization data. Thus, phases in the $Sr_2In_{1-x}Sn_xSbO_6$ ($0 \leq x \leq 0.3$) series all exhibit bulk diamagnetic behavior and have no magnetic transitions, as expected, since no magnetic elements are present.

3.2.2 Band Gaps and Band Structures

The band gap for each composition in the $Sr_2In_{1-x}Sn_xSbO_6$ ($0 \leq x \leq 0.3$) series was determined from the diffuse reflectance spectra collected. The pseudo-absorbance, transferred from reflectance using the Kubelka-Munk function, is plotted against photon energy (eV) in Figure 6. The optical transitions were then analyzed based on Tauc plots. There are two obvious transitions in the samples, denoted as transitions 1 and 2, and the resulting visual appearances are a consequence of the superposition of these two optical transitions (Figure 6). Transition 1 lies approximately between 3.5 and 4.0 eV and exhibits a sharp shape that is characteristic of a direct band gap. Hence the direct-transition equation was applied while extracting the values from Tauc plots, as shown in the upper embedded panel in Figure 6. In contrast, transition 2 in the low photon energy regime has a much shallower shape, which is characteristic for indirect transitions. Thus, the indirect-transition equation was employed to calculate the gap values, as shown in the lower embedded panel in Figure 6. In addition, the shape of absorbance is also related to the electronic density of states at the upper part of the valence band and the lower part of the conduction band. According to our DFT calculations, the valence band maximum (VBM) mainly consists of O-2p orbitals, whereas the conduction band minimum (CBM) is dominated by 5s and 5p orbitals of Sb, as expected. One extra feature to address for transition 2 is that the pseudo-absorbance does become significantly stronger upon increasing the Sn-dopant concentration, consistent with the darker appearance of the sample powder as *x* increases. In general, the values of both direct transition 1 and indirect transition 2 show a decreasing trend with increasing Sn^{4+} content.

To further characterize these two observed transitions, the calculated band structures and densities of electronic states (DOS) for the undoped parent phase Sr_2InSbO_6 were employed (Figure 7). Spin-orbit coupling (SOC) applied for In and Sb hardly impacts the calculated band structures. A

calculated direct bandgap of ~ 2 eV is clearly observed at the Γ point, corresponds to the experimentally observed direct transition 1 of ~ 4 eV. It is not surprising since DFT calculations commonly underestimate band gaps for compounds containing main group elements. Indirect transition 2 may arise from some intermediate states which are absent in the calculated band structures, consistent with its weak absorption behavior observed in diffuse reflectance spectra.

We note that during the preparation of this manuscript, two papers containing DFT band structures (and optical properties) of Sr_2InSbO_6 were published. In the work by Y. Xie *et al.*[25], the structural model employed in their DFT calculations is a monoclinic unit cell ($P2_1/c$) with lattice parameters different from ours (Table S1). In addition, the synthetic conditions of their samples are different from ours, which may cause different observed optical behavior. M.A. Amin *et al.* report the calculated band structures of Sr_2InSbO_6[26] as well, which in general agree with our results (a direct band gap observed at the Γ point) except the value of their calculated gap (2.55 eV) is slightly larger than our experimental one (~ 2 eV). This difference may arise from the face-centered cubic cell (*Fm*-3*m*) they used in their calculations, while we used the monoclinic cell ($P2_1/n$, slightly distorted from cubic) for our DFT calculations. Further interpretation of these observed optical transitions and band structures may be of interest in future work.

3.2.3 Carrier-type characterization

The Sb-Mössbauer results suggest that there is a small increase in the local electron density around the ^{121}Sb nucleus, as reflected by the decrease in isomer shift upon Sn^{4+}-for-In^{3+} substitution. Thus, in order to further confirm the type of carriers in our materials, the hot-point probe measurement was conducted on the sintered pellet of each composition in the $Sr_2In_{1-x}Sn_xSbO_6$ ($0 \leq x \leq 0.3$) series. A Bi_2Se_3 single crystal, which is always an *n*-type semiconductor,

was used as a reference. The hot-point probe measurement conducted on the Bi_2Se_3 single crystal showed a steady positive reading for voltage on the multimeter. Despite the fact that the readings were a little bit fluctuating, all three Sn-doped samples (x = 0.1, 0.2, 0.3) showed positive readings for voltage as well, consistent with those shown by the Bi_2Se_3 single crystal, proving that the carriers in our Sn-doped materials are *n*-type. In addition, the undoped parent phase Sr_2InSbO_6 just gave a reading around 0, which means that it is neither a strongly *p*- nor a strongly *n*-type semiconductor. Hence combining the results from Mössbauer spectroscopy and hot-point probe measurement, it is valid to conclude that Sn^{4+} is partially substituted into the In^{3+} site and produces *n*-type carriers in our $Sr_2In_{1-x}Sn_xSbO_6$ materials.

The fact that the Sn^{4+} dopant acts as an electron-donor in our materials suggests that the Sn 5s states (E_D) should have lower energy than the Sb 5s states, as illustrated in the simple qualitative energy level diagram (Figure 8). Therefore, with elevated Sn concentration, the pseudo-absorbance in the lower energy regime becomes stronger and the concentration of n-type carriers in our materials increases.

4. Conclusions

The double perovskite Sr_2InSbO_6 and its Sn^{4+}-for-In^{3+} substituted phases were prepared via conventional high-temperature ceramic synthesis and characterized from structural, magnetic, optical and carrier-type points of view. The perfect fits of single line absorption both in ^{121}Sb and ^{119}Sn Mössbauer spectra to a single-site occupancy model unambiguously confirm the rigid ordering between two distinct B-cation sites in the lattice. The undoped parent phase Sr_2InSbO_6 adopts a typical rock-salt type double perovskite structure and crystallizes in monoclinic symmetry

(space group $P2_1/n$). The Sn^{4+} dopant is shown to go to the In^{3+} site only, and the parent phase crystal structure is conserved in all the Sn-doped phases, with continuous changes in lattice parameters. The upper doping limit of the system is found to be 30%, beyond this composition threshold, an orthorhombic secondary phase $Sr_2Sb_2O_7$ starts to occur. Magnetization data collected from all the phases shows that they all exhibit bulk diamagnetic behavior and have no magnetic transitions. The diffuse reflectance spectra collected indicate that a strong direct transition and a weak indirect transition are present in all the materials. The calculated band structure of Sr_2InSbO_6 suggests that the strong direct transition should be attributed to the direct band gap observed at the Γ point, while the weak indirect transition may arise from some absent intermediate states. In general, the direct band gap decreases, and the pseudo-absorbance of the indirect transition becomes significantly stronger, with increasing Sn^{4+}content. The doped materials are confirmed to be *n*-type by both the decrease in isomer shift in Sb-Mössbauer and the positive readings for voltage on the multimeter in hot-point probe measurements. In conclusion, by partially substituting In^{3+} with Sn^{4+} in Sr_2InSbO_6 double perovskite, *n*-type semiconductors can be fabricated.

Supporting Information

The Supporting Information is available from the publisher or from the authors upon valid request.

Acknowledgements

This research was primarily done at Princeton University, supported by the US Department of Energy, Division of Basic Energy Sciences, grant number DE-FG02-98ER45706. The Mössbauer spectral work by DHM and RPH at Oak Ridge National Laboratory was supported by the U.S.

Department of Energy, Office of Science, Office of Basic Energy Sciences, Materials Sciences and Engineering Division.

Conflict of Interest

The authors declare no conflict of interest.

References

[1] P. Schiffer, A.P. Ramirez, W. Bao, S.W. Cheong, Low Temperature Magnetoresistance and the Magnetic Phase Diagram of $La_{1-x}Ca_xMnO_3$, Phys. Rev. Lett. 75 (1995) 3336. https://doi.org/10.1103/PhysRevLett.75.3336.

[2] J.G. Bednorz, K.A. Müller, Possible high T_c superconductivity in the Ba−La−Cu−O system, Zeitschrift Für Phys. B Condens. Matter. 64 (1986) 189–193. https://doi.org/10.1007/BF01303701.

[3] R.E. Cohen, Origin of ferroelectricity in perovskite oxides, Nature. 358 (1992) 136. https://doi.org/10.1038/358136a0.

[4] P. Lacorre, F. Goutenoire, O. Bohnke, R. Retoux, Y. Lallgant, Designing fast oxide-ion conductors based on $La_2Mo_2O_9$, Nature. 404 (2000) 856–858. https://doi.org/10.1038/35009069.

[5] R. Asahi, T. Morikawa, T. Ohwaki, K. Aoki, Y. Taga, Visible-Light Photocatalysis in Nitrogen-Doped Titanium Oxides, Science. 293 (2001) 269–271. https://doi.org/10.1126/science.1061051.

[6] M.A. Peña, J.L.G. Fierro, Chemical Structures and Performance of Perovskite Oxides, Chem. Rev. 101 (2001) 1981–2018. https://doi.org/10.1021/cr980129f.

[7] I. Chung, B. Lee, J. He, R.P.H. Chang, M.G. Kanatzidis, All-solid-state dye-sensitized solar cells with high efficiency, Nature. 485 (2012) 486–489. https://doi.org/10.1038/nature11067.

[8] J. Sunarso, S.S. Hashim, N. Zhu, W. Zhou, Perovskite oxides applications in high temperature oxygen separation, solid oxide fuel cell and membrane reactor: A review, Prog. Energy Combust. Sci. 61 (2017) 57–77. https://doi.org/10.1016/J.PECS.2017.03.003.

[9] A. Hirohata, K. Yamada, Y. Nakatani, L. Prejbeanu, B. Diény, P. Pirro, B. Hillebrands, Review on spintronics: Principles and device applications, J. Magn. Magn. Mater. 509 (2020) 166711. https://doi.org/10.1016/J.JMMM.2020.166711.

[10] U. Wittmann, G. Rauser, S. Kemmler- Sack, Über die Ordnung von B^{III} und M^V in Perowskiten vom Typ $A^{II}{}_2B^{III}M^VO_6$ (A^{II} = Ba, Sr; M^V = Sb, Nb, Ta), Zeitschrift Für Anorg. Und Allg. Chemie. 482 (1981) 143–153. https://doi.org/10.1002/ZAAC.19814821117.

[11] A. Tauber, S.C. Tidrow, R.D. Finnegan, W.D. Wilber, HTSC substrate and buffer layer compounds, A_2MeSbO_6 where A = Ba, Sr and Me = Sc, In and Ga, Phys. C Supercond. 256 (1996) 340–344. https://doi.org/10.1016/0921-4534(95)00661-3.

[12] A.E. Lavat, E.J. Baran, IR-spectroscopic characterization of $A_2BB'O_6$ perovskites, Vib. Spectrosc. 32 (2003) 167–174. https://doi.org/10.1016/S0924-2031(03)00059-6.

[13] W.T. Fu, D.J.W. IJdo, X-ray and neutron powder diffraction study of the monoclinic perovskites Sr_2MSbO_6 (M=In, Y), Solid State Commun. 134 (2005) 177–181. https://doi.org/10.1016/J.SSC.2005.01.018.

[14] R. Shaheen, J. Bashir, Crystal structure of A_2InSbO_6 (A = Ca, Sr, Ba) ordered double perovskites, Solid State Sci. 12 (2010) 605–609. https://doi.org/10.1016/J.SOLIDSTATESCIENCES.2010.01.011.

[15] H. Rietveld, A profile refinement method for nuclear and magnetic structures, J. Appl. Crystallogr. 2 (1969) 65–71. https://doi.org/10.1107/S0021889869006558.

[16] A.Y. Tarasova, L.I. Isaenko, V.G. Kesler, V.M. Pashkov, A.P. Yelisseyev, N.M. Denysyuk, O.Y. Khyzhun, Electronic structure and fundamental absorption edges of KPb_2Br_5, $K_{0.5}Rb_{0.5}Pb_2Br_5$, and $RbPb_2Br_5$ single crystals, J. Phys. Chem. Solids. 73 (2012) 674–682. https://doi.org/10.1016/J.JPCS.2012.01.014.

[17] P. Blaha, K. Schwarz, G.K.H. Madsen, D. Kvasnicka, J. Luitz, R. Laskowsk, F. Tran, L. Marks, L. Marks, WIEN2k: An Augmented Plane Wave Plus Local Orbitals Program for Calculating Crystal Properties, Techn. Universitat, 2019. https://www.scholars.northwestern.edu/en/publications/wien2k-an-augmented-plane-wave-plus-local-orbitals-program-for-ca (accessed July 30, 2021).

[18] E. Wimmer, H. Krakauer, M. Weinert, A.J. Freeman, Full-potential self-consistent linearized-augmented-plane-wave method for calculating the electronic structure of molecules and surfaces: O_2 molecule, Phys. Rev. B. 24 (1981) 864–875. https://doi.org/https://doi.org/10.1103/PhysRevB.24.864.

[19] J.P. Perdew, Y. Wang, Accurate and simple analytic representation of the electron-gas correlation energy, Phys. Rev. B. 45 (1992) 13244–13249. https://doi.org/https://doi.org/10.1103/PhysRevB.45.13244.

[20] R.D. King-Smith, D. Vanderbilt, Theory of polarization of crystalline solids, Phys. Rev. B. 47 (1993) 1651–1654. https://doi.org/https://doi.org/10.1103/PhysRevB.47.1651.

[21] S. Klenner, J. Bönnighausen, J. Guo, Z. Yang, S. Pan, R. Pöttgen, A ^{119}Sn Mössbauer-spectroscopic characterization of the diamagnetic birefringence material $Sn_2B_5O_9Cl$, Zeitschrift Fur Naturforsch. - Sect. B J. Chem. Sci. 74 (2019) 879–883. https://doi.org/10.1515/znb-2019-0173.

[22] R.P. Hermann, Mößbauer Spectroscopy, in Handbook of Solid State Physics., First Edition, edited by R. Dronkowski, S. Kikkawa, and A. Stein (2017) .

[23] P.E. Lippens, Mössbauer isomer shifts of crystalline antimony compounds, Solid State Commun. 113 (2000) 399–403. https://doi.org/10.1016/S0038-1098(99)00501-3.

[24] P.E. Lippens, J. Olivier-Fourcade, J.C. Jumas, Interpretation of the ^{119}Sn Mössbauer parameters, Hyperfine Interact. 126 (2000) 137–141. https://doi.org/10.1023/A:1012653014106.

[25] Y. Xie, X. Geng, Y. Wang, J. Guo, Y. Lu, Q. Lv, Z. Ma, D. Zhang, J. Zhao, B. Deng, R. Yu, An efficient far-red emission Sr_2InSbO_6 :Mn^{4+}, M (M= Li^+, Na^+,and K^+) phosphors for plant cultivation LEDs, J. Am. Ceram. Soc. 105 (2022) 1300–1317. https://doi.org/10.1111/jace.18115.

[26] M.A. Amin, G. Nazir, Q. Mahmood, J. Alzahrani, N.A. Kattan, A. Mera, H. Mirza, A. Mezni, M.S. Refat, A.A. Gobouri, T. Altalhi, Study of double perovskites X_2InSbO_6 (X = Sr, Ba) for renewable energy; alternative of organic-inorganic perovskites, J. Mater. Res. Technol. 18 (2022) 4403- 4412. https://doi.org/10.1016/j.jmrt.2022.04.114.

Table 1. Structural parameters and crystallographic positions from the refinement of lab X-ray powder diffraction data collected from $Sr_2In_{0.9}Sn_{0.1}SbO_6$ at 300 K.

Atoms	*x*/*a*	*y*/*b*	*z*/*c*	S.O.F.	U_{iso} equiv. ($Å^2$)
Sb1	0	0.5	0	1	0.0028
In1	0.5	0	0	0.9	0.0015
Sr1	0.4962(6)	0.47496(13)	0.2501(6)	1	0.00788
O1	0.2025(29)	0.2290(27)	0.0305(19)	1	0.0028
O2	0.2696(26)	0.7061(31)	0.0282(21)	1	0.0026
O3	0.5742(23)	0.0083(9)	0.2680(18)	1	0.0001
Sn1	0.5	0	0	0.1	0.0015

$Sr_2In_{0.9}Sn_{0.1}SbO_6$ space group $P2_1/n$ (#14)
Formula weight: 508.204 g mol^{-1}, Z = 2
a = 5.72318(4) Å, b = 5.72170(4) Å, c = 8.08907(6) Å, β = 89.9288(5) °, V = 264.8871(21) $Å^3$
Radiation source: Cu Kα
Temperature: 300 K
wR = 9.090%; GOF = 1.47

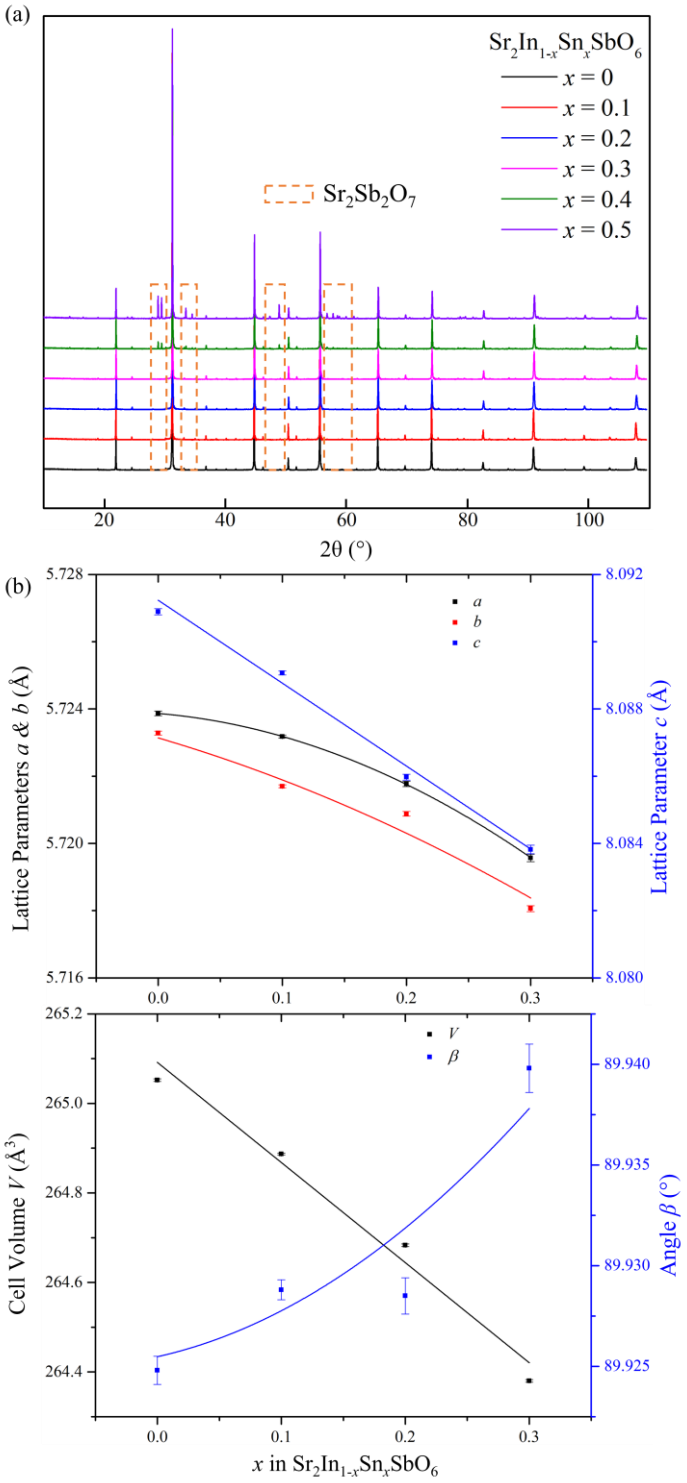

Figure 1. (a) Stacked lab X-ray powder diffraction patterns for compositions of the $Sr_2In_{1-x}Sn_xSbO_6$ series, with orange boxes highlighting the growth of peaks representing the impurity phase $Sr_2Sb_2O_7$; (b) lattice parameter *a*, *b*, *c*, cell volume *V* and angle β plotted for each composition of the $Sr_2In_{1-x}Sn_xSbO_6$ series.

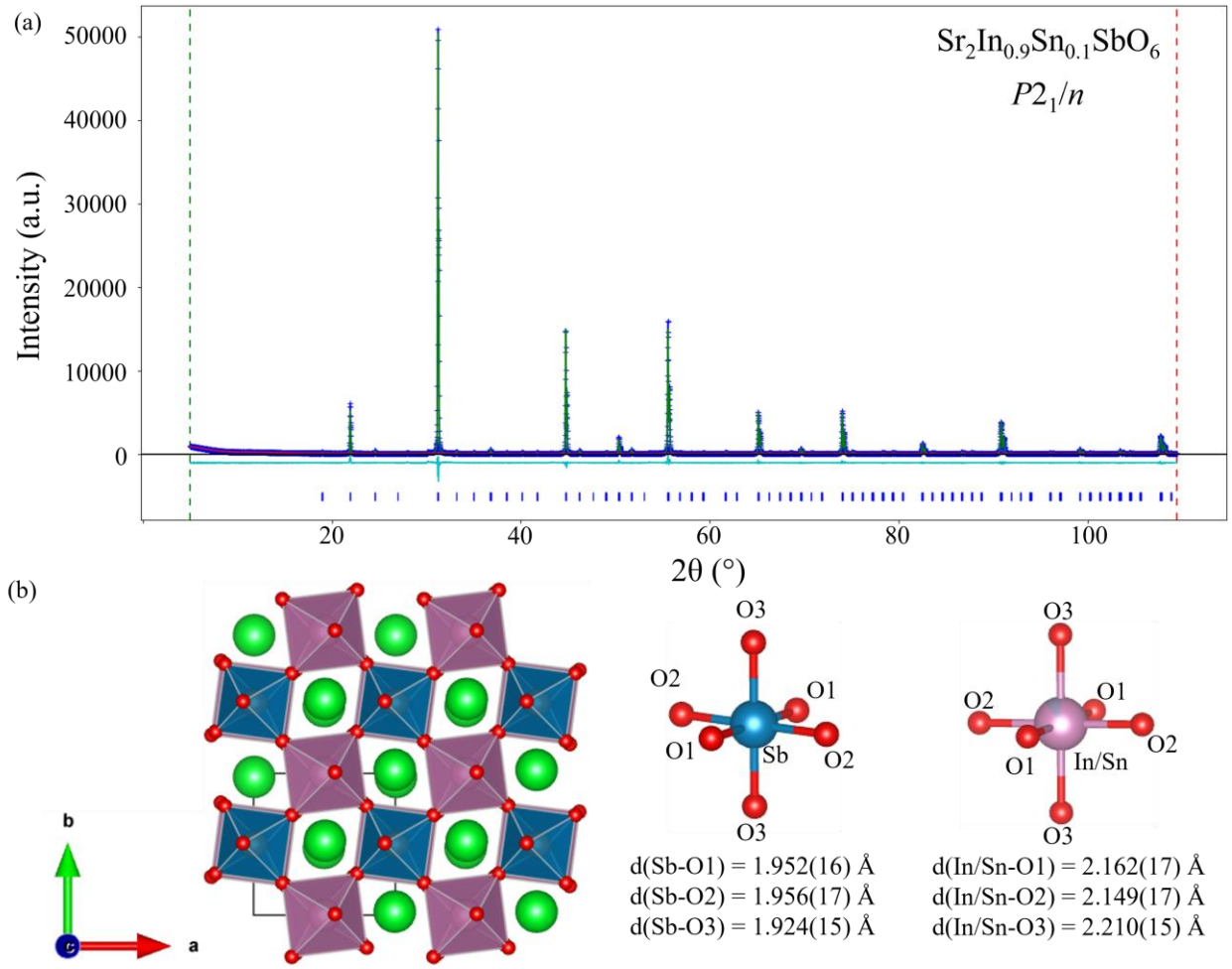

Figure 2. (a) Observed (blue), calculated (green), and difference (cyan) plots from the Rietveld refinement of $Sr_2In_{0.9}Sn_{0.1}SbO_6$ (space group $P2_1/n$) against the lab pXRD data; (b) The structural model for $Sr_2In_{0.9}Sn_{0.1}SbO_6$ together with selected bond lengths for the SbO_6 octahedron and the $(In/Sn)O_6$ octahedron.

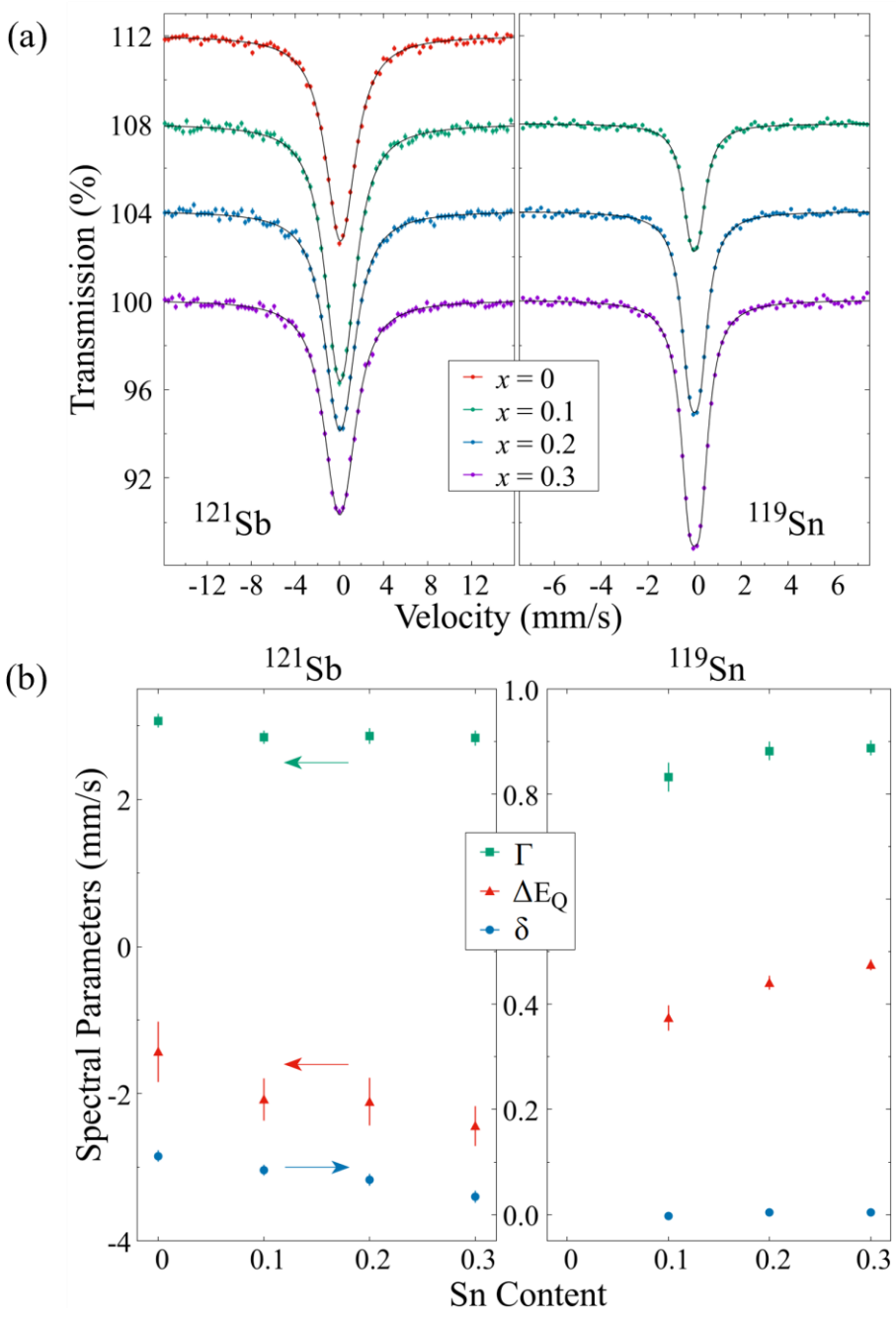

Figure 3. (a) (Left) ^{121}Sb- and (Right) ^{119}Sn-Mössbauer spectra of $Sr_2In_{1-x}Sn_xSbO_6$ for the indicated *x*, measured at room temperature. Solid lines are fits to a single site model; (b) Spectral parameters for the fits to (Left) ^{121}Sb- and (Right) ^{119}Sn-Mössbauer spectra indicating trends of linewidth (Γ), quadrupole splitting (ΔE_Q), and isomer shift (δ) upon increasing Sn content *x* in $Sr_2In_{1-x}Sn_xSbO_6$. Arrows indicate the applicable y-axis for the respective datasets.

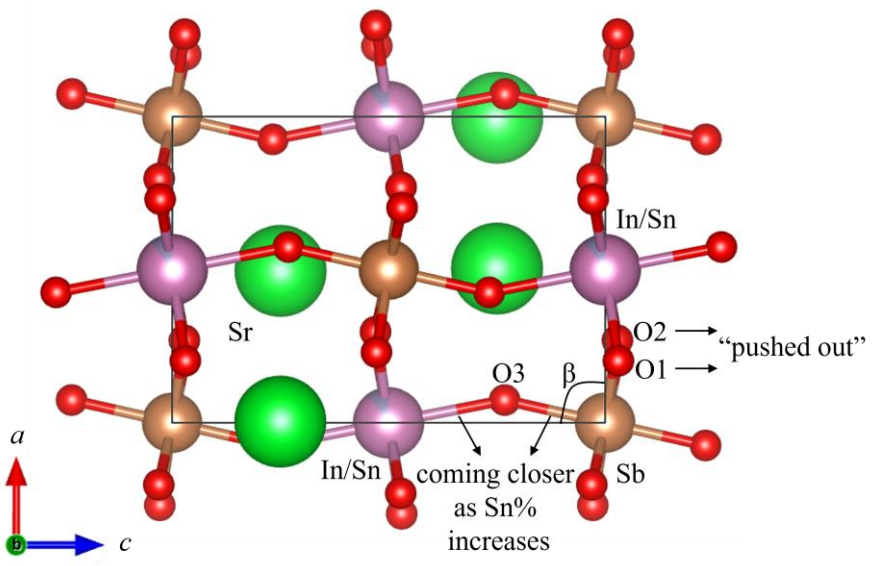

Figure 4. A side-view of the unit cell along the *b* axis of the $Sr_2In_{1-x}Sn_xSbO_6$ series.

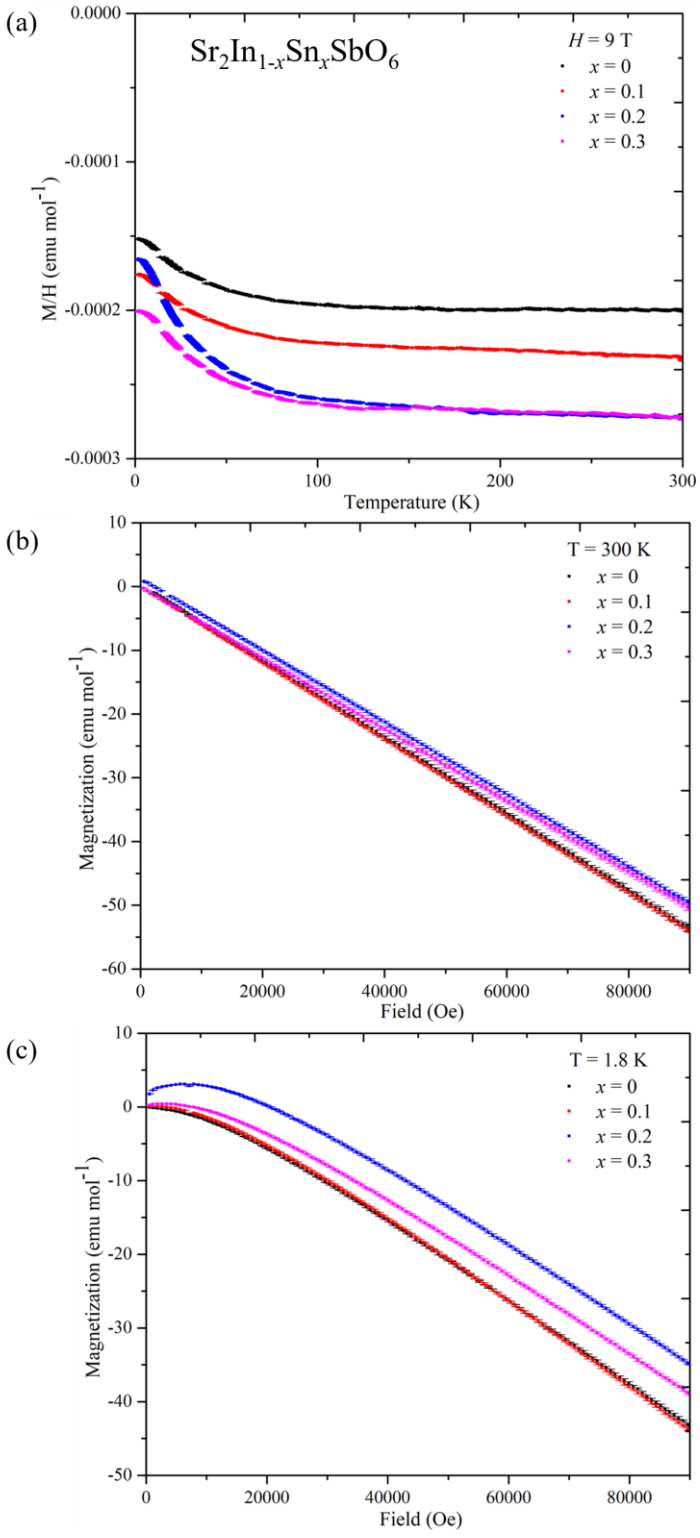

Figure 5. (a) The temperature-dependent magnetization data collected under an applied field of H = 9 T; The field-dependent magnetization data collected at (b) 300 K and (c) 1.8 K for each composition of the $Sr_2In_{1-x}Sn_xSbO_6$ ($0 \leq x \leq 0.3$) series.

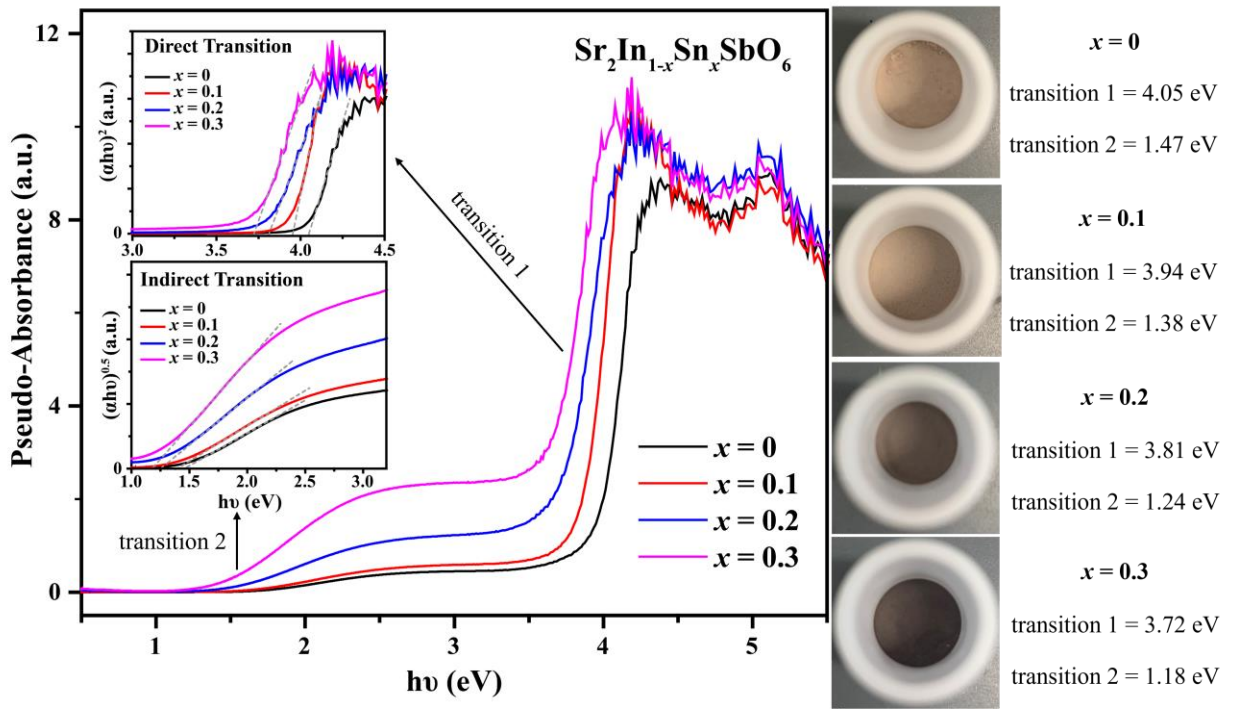

Figure 6. The diffuse reflectance spectra of the $Sr_2In_{1-x}Sn_xSbO_6$ ($0 \leq x \leq 0.3$) series and the calculated values of transition 1 and 2 from Tauc plots.

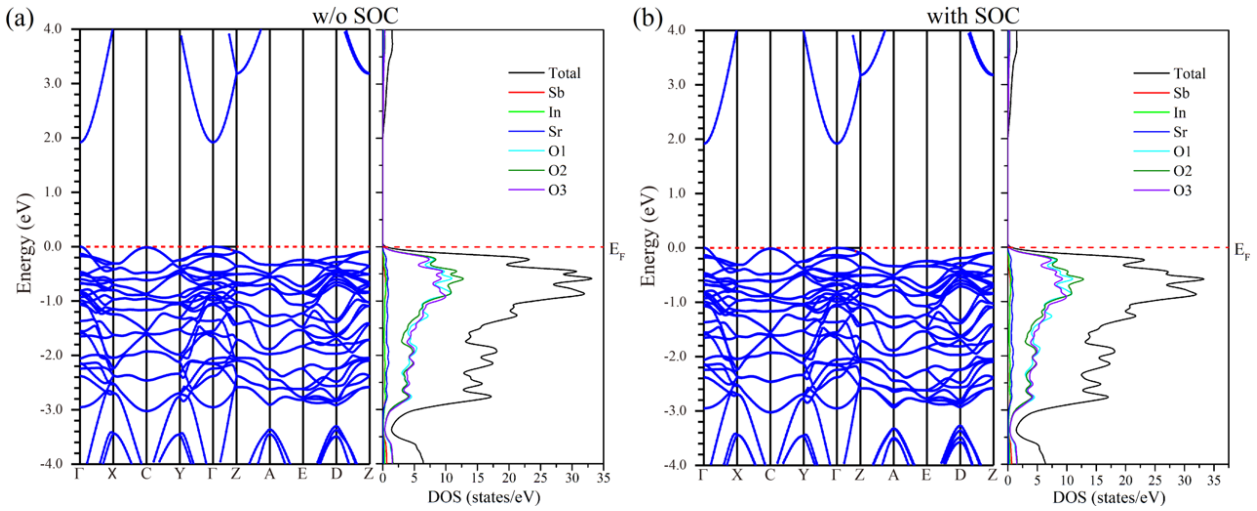

Figure 7. The calculated band structures and densities of electronic states (DOS) (a) without and (b) with spin-orbit coupling (SOC) for the undoped parent phase Sr_2InSbO_6.

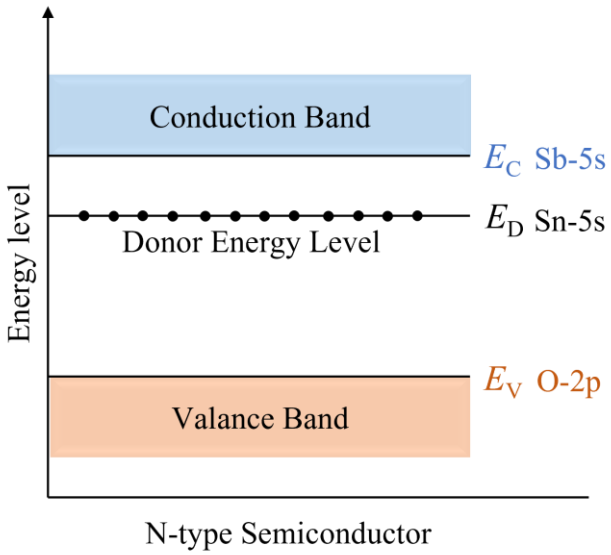

Figure 8. The qualitative energy level diagram of the *n*-type semiconductor $Sr_2In_{1-x}Sn_xSbO_6$ series.

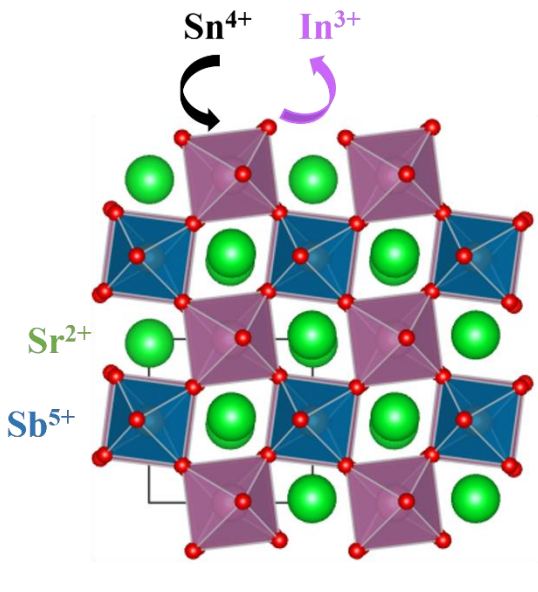

$Sr_2In_{1-x}Sn_xSbO_6$

$P2_1/n$

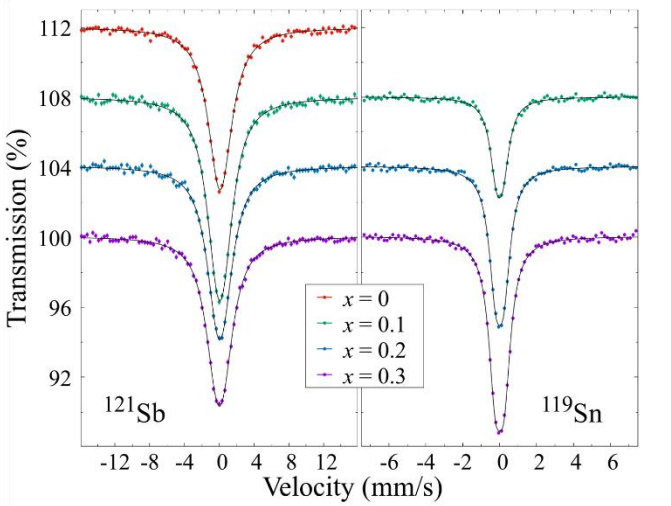

Single-site occupancy confirmed by Mössbauer spectra

A series of *n*-type oxide double perovskite semiconductors, $Sr_2In_{1-x}Sn_xSbO_6$ ($0 \leq x \leq 0.3$) has been synthesized and fully characterized. Mössbauer spectroscopy are employed to investigate the B-site cation ordering because this issue cannot be resolved by conventional diffraction techniques alone.